Electronic Transport and Raman Scattering in Size-Controlled Nanoperforated Graphene

Myungwoong Kim, Nathaniel S. Safron, Eungnak Han, Michael S. Arnold,* and Padma Gopalan*

Department of Materials Science and Engineering, University of Wisconsin-Madison, Madison, Wisconsin 53706, United States

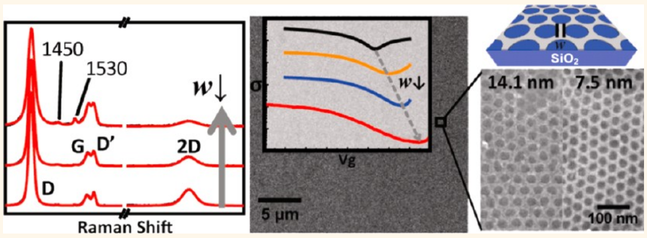

ABSTRACT We demonstrate the fabrication and study of the structure–property relationships of large-area (>1 cm^2) semiconducting nanoperforated (NP) graphene with tunable constriction width (w = 7.5–14 nm), derived from CVD graphene using block copolymer lithography. Size-tunable constrictions were created while minimizing unintentional doping by using a dual buffer layer pattern-transfer method. An easily removable polymeric layer was sandwiched between an overlying silicon oxide layer and the underlying graphene. Perforation-size was controlled by overetching holes in the oxide prior to pattern transfer into graphene while the polymer protected the graphene from harsh conditions during oxide etching and lift off. The processing materials were removed using relatively mild solvents yielding the clean isolation of NP graphene and thereby facilitating Raman and electrical characterization. We correlate the D to G ratio as a function of w and show three regimes depending on w relative to the characteristic Raman relaxation length. Edge phonon peaks were also observed at 1450 and 1530 cm^{-1} in the spectra, without the use of enhancement methods, due to high density of nanoconstricted graphene in the probe area. The resulting NP graphene exhibited semiconducting behavior with increasing ON/OFF conductance modulation with decreasing w at room temperature. The charge transport mobility decreases with increasing top-down reactive ion etching. From these comprehensive studies, we show that both electronic transport and Raman characteristics change in a concerted manner as w shrinks.

KEYWORDS: semiconducting graphene · block copolymer lithography · large-area nanopatterning · Raman · field-effect transistor

Graphene has emerged as a new material platform for ultrafast nanoelectronics,[1,2] transparent conductors,[3] and flexible electronics[4] due to its exceptionally high charge mobility potentially exceeding 200,000 $cm^2/(V\cdot s)$, and excellent mechanical and optical properties.[5−8] However, due to its inherent zero band gap, the applicability of graphene has been limited in semiconducting electronics.[8] One solution is to reduce the critical dimension of graphene below 20 nm, to open up an effective band gap due to the quantum confinement effect. Two geometries for semiconducting graphene are (i) nanoribbons (GNRs) and (ii) nanoperforated (NP)[9,10] or antidot lattices. Sub-20 nm semiconducting GNRs have been fabricated using various methods such as e-beam lithography,[11] unzipping carbon nanotubes,[12,13] etching graphene with nanowire etch mask,[14] and the chemical exfoliation of graphite.[15] However, two factors limiting the applicability of GNRs are challenges in scaling for mass-production and difficulties in alignment and placement into circuit geometries.[16] NP graphene is essentially a perforated membrane with nanoconstrictions of graphene between holes, that can be fabricated using a variety of techniques such as e-beam lithography,[17] nanosphere lithography,[18,19] nanoimprint lithography,[20] and block copolymer lithography,[9,10] resulting in an effective electronic band gap, which scales inversely with nanoconstriction width (w). We are specifically interested in using block copolymer (BCP) lithography as a means for fabricating NP graphene as it can be scaled to large-area substrates with high-fidelity of patterning, is compatible with conventional semiconductor manufacturing processes, and gives access to sub-20 nm features.[21]

Despite successful fabrication of NP graphene by various methods, detailed characterization is lacking. Our goal in this work is to fabricate and characterize a large-area NP graphene and characterize the electronic transport and Raman scattering in

* Address correspondence to pgopalan@cae.wisc.edu, msarnold@wisc.edu.

Received for review July 28, 2012 and accepted October 31, 2012.

10.1021/nn3033985

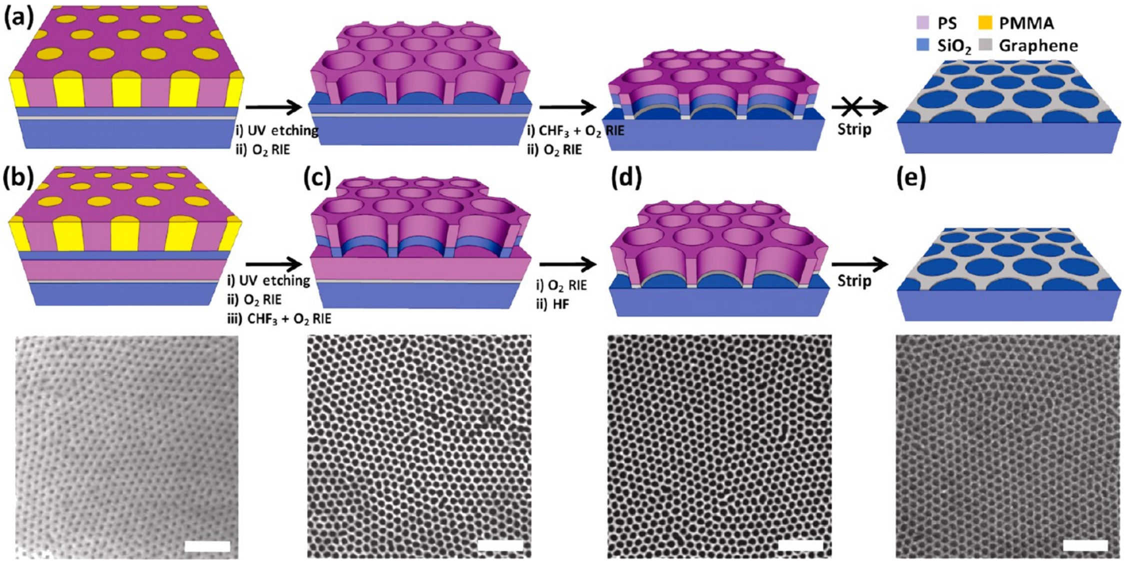

Figure 1. **Schematic depicting fabrication of nanoperforated graphene (a) *via* previous process[9] and (b–e) *via* dual buffer layer process. Top-down SEM images of (b) thin film of perpendicularly oriented PMMA cylinder arrays in PS matrix on silicon oxide layer, (c) hole arrays formed *via* removal of PMMA perpendicular cylinders and subsequent O_2 and $CHF_3 + O_2$ plasma etching, (d) hole arrays in PS matrix after O_2 plasma etching and subsequent removal of silicon oxide hardmask with 1 wt % HF aqueous solution, (e) patterned graphene after stripping PS matrix (scale bars, 200 nm).**

these size-controlled NP structures created by top-down etching. Lack of complete characterization of NP graphene is mainly due to two reasons. Much of the work so far has been done on small exfoliated pieces of graphene making uniform Raman characterization over large area challenging, and second in most top-down etching methods it is difficult to obtain stand-alone NP graphene as the patterned structures cannot be effectively isolated from the processing materials. Hence in all the top-down etching reports in the literature so far there are no reports of Raman characterization of NP graphene or how the mobility changes as a function of constriction width *w*. Much of the focus has been on studying ON/OFF conductance modulation as a function of *w*. In our previous publication (Figure 1a),[9] we did discuss the effect of RIE etchants on edge functionalization and doping levels mainly using electrical characterization. In that work we used a silicon oxide buffer layer on graphene to aid in wetting of the BCP. The oxide layer was modified with a random copolymer to induce perpendicular domain orientation in the overlying P(S-*b*-MMA) domains. Pattern transfer to the underlying oxide and graphene was achieved using a CHF_3 plasma and subsequently an O_2 plasma. Etching graphene with strong electron-withdrawing heteroatom-containing gases results in dangling bonds on the edges, which in turn alters the electronic properties. Overetching with CHF_3 to transfer the BCP pattern to silicon oxide and graphene inevitably led to heavy doping of graphene which could not be completely reversed by subsequent O_2 plasma etching.[9] Furthermore, the resulting NP graphene was covered with silicon oxide and the cross-linked PS template. The removal of the cross-linked PS template and the oxide was complicated as any reagents used to strip these layers resulted in breaking up the patterned graphene, as well. Hence direct Raman characterization of the NP graphene was complicated owing to difficulty in removing the overlying oxide buffer layer.

To address these challenges, we have developed here a method that uses "dual buffer layers" between the BCP template and CVD grown graphene to fabricate large-area NP graphene (Figure 1b–e). In this process, graphene is sequentially covered by a polystyrene (PS) layer followed by a silicon oxide buffer layer. The oxide layer acts as a hardmask, whereas the PS layer acts as a protective layer to prevent the direct etching of graphene by the fluorine gas plasma. By first patterning holes using a BCP template in the oxide hardmask, it is then possible to controllably enlarge the hole in the underlying PS layer. This geometry also allows clean isolation of patterned graphene from the polymeric template, as the un-cross-linked PS buffer layer can be easily removed by exposure to solvents that dissolve PS. In the absence of the PS buffer layer, the PS template left from the BCP film is highly cross-linked due to exposure to O_2 plasma and hence cannot be removed by common solvents.[22] Generally in BCP lithography, sonication in organic solvent such as *N*-methyl-2-pyrrolidone (NMP) or toluene, Piranha solution, or O_2 plasma have been used to remove plasma-treated PS residues.[23,24] However, these methods are not applicable to graphene on SiO_2/Si due to the weak interactions between graphene and the substrate leading to lift-off and oxidation of graphene. In contrast, in the dual buffer layer process, the silicon oxide hardmask shields the top-surface of the PS buffer from cross-linking by O_2 plasma. Therefore, it can be removed in common solvents after pattern transfer to the underlying graphene without damage to the graphene and SiO_2/Si substrate. As a result it removes all the overlying layers, that is, the oxide buffer layer and the cross-linked PS template from BCP, leaving just the patterned graphene on the oxide substrate.

We used a single layer graphene (SLG) synthesized *via* chemical vapor deposition (CVD) as the starting material to create large-area (>1 cm^2) NP graphene. Using the dual buffer layer process, CVD graphene was successfully nanopatterned to sub-10 nm constriction width and isolated from the processing materials. Resulting NP graphene exhibited small-gap semiconductor-like behavior with an increased ON/OFF conductance modulation at room temperature as *w* shrinks. The severe uncontrolled p-doping during the plasma etching process was effectively minimized. Owing to the high density of graphene nanostructures in the Raman probe area, two well-defined sharp peaks at ~1450 and ~1530 cm^{-1} due to the zigzag and the arm-chair edges respectively were observed without any Raman enhancement.[25] In this comprehensive study we correlate the edge disorder studied by Raman scattering with electronic transport measurements as a function of *w*, to provide insight into the limitations of top-down etching methods.

RESULTS AND DISCUSSIONS

Fabrication of NP Graphene with Varying *w*. Figure 1b–e depicts the dual buffer layer process on a large-area CVD grown graphene (>1 cm^2) with the corresponding top-down SEM images. A preassembled P(S-*b*-MMA) thin film deposited on a silicon oxide/PS/graphene substrate shows a periodic hexagonal array of perpendicular PMMA cylinders (dark dots in the SEM image) surrounded by the PS matrix (bright matrix in SEM image, Figure 1b). After removing the PMMA domains by UV irradiation and acetic acid treatment to create hole arrays, O_2 plasma etching and subsequent $CHF_3 + O_2$ mixed plasma etching was used to transfer the hole arrays using the residual PS template to the oxide buffer layer (Figure 1c). Upon subsequent O_2 plasma etching, the oxide buffer layer was used as a hardmask to pattern transfer holes through the underlying PS buffer to graphene. Since the PS buffer layer is shielded from the plasma by the oxide buffer layer, the thickness reduction of the PS layer is avoided, hence allowing longer etching time for hole enlargement in the PS layer by lateral etching. The oxide layer was then removed by immersion in 1 wt % HF aqueous solution for ~10 s. Under these mild conditions, the measured etch rates of e-beam evaporated (oxide buffer layer) and thermally grown silicon oxides were ~2 nm/sec and ~3 nm/min, respectively. Hence, the selective removal of the oxide on the PS layer was feasible. Figure 1d shows that the hole arrays were well-defined in the PS layer after removal of the oxide hardmask. Finally, patterned graphene samples were treated with warm (50–60 °C) organic solvents (*N*-methyl-2-pyrrolidone and tetrahydrofuran) or commercial photoresist stripper (AZ-300T or AZ-400T) to remove the residual PS buffer layer and to isolate the patterned graphene. The use of these relatively inert solvents to remove the polymeric templates as against plasma gases is highly advantageous, as graphene is very susceptible to doping by nearly all species. Supporting Information, Figure S1 shows the large-area (25 μm × 25 μm) top-down SEM image of the resulting NP graphene (>1 cm^2) fabricated by the dual buffer layer process.

The etching time was varied in the final O_2 plasma step to fabricate NP samples with systematic variation in *w*. The hole size can be enlarged in the PS buffer layer by lateral etching guided by the overlying oxide hardmask, leading to a well-controlled *w* in the patterned graphene. Figure 2a–d displays the top-down SEM images of the resulting NP graphene with increasing etching time resulting in decrease in *w*, from 14.1 to 7.5 nm.

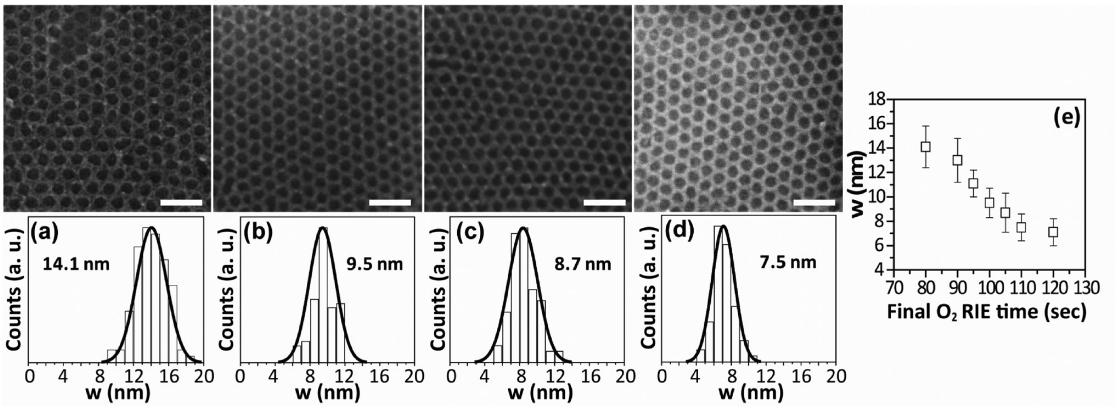

Figure 2. Top-down SEM images (a–d) of nanoperforated graphene with a gradual variation in *w* with the corresponding histograms (scale bars, 100 nm), as a function of final O_2 etching time. (e) The mode value of *w*, analyzed from 0.5 μm × 0.5 μm SEM images and histograms using the ImageJ image analysis program with the method described in Supporting Information, Figure S5, is then plotted as a function of final O_2 etching time.

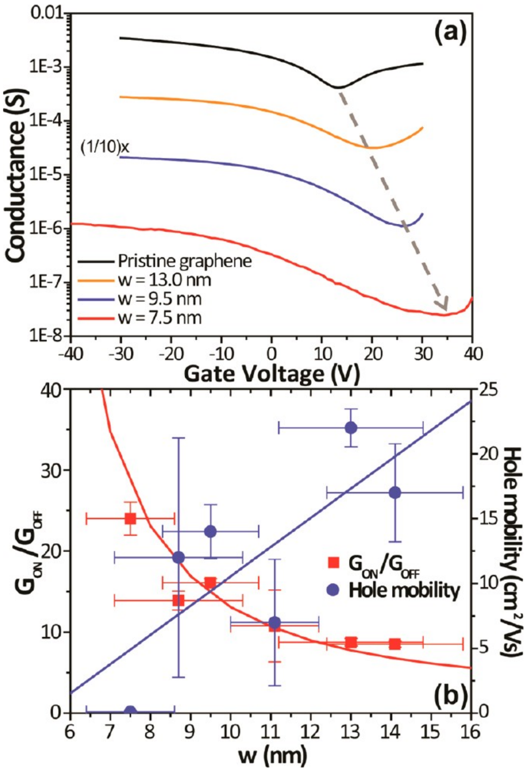

Figure 3. Electrical characterization of nanoperforated graphene FETs. (a) Conductance as a function of gate bias at room temperature with changing *w*. (b) G_{ON}/G_{OFF} (left *y*-axis) and hole mobility (right *y*-axis) as a function of *w*. Red solid line is a fitting result of G_{ON}/G_{OFF} data with exponential function presented in the main text. Blue solid line is a guide to hole mobility data.

This process gives good control over *w* with small (<2 nm, Figure 2e) standard deviations. (Note that line edge roughness and edge defects are beyond the resolution of SEM.) In all cases, the center-to-center distance between holes is ~36.5 nm which is defined by the periodicity of the BCP.

Changes in Electrical Properties as a Function of *w*. To characterize the electrical properties of NP graphene, large-area field effect transistors (FETs) on 89 nm SiO_2/Si(p++) substrate, which acts as the back gate, were defined by shadow masking gold electrodes (15 μm × 120 μm, channel length × width) on NP graphene. Measurements on unpatterned graphene FET show modest p-doped (Dirac point ≈ 13 V) ambipolar behavior with an ON/OFF conductance modulation (G_{ON}/G_{OFF}) of ~5 in the range of ±30 V at room temperature (Figure 3a). For the NP graphene, both p-doping and the G_{ON}/G_{OFF} increase as *w* decreases. The increase in p-doping is likely due to increase in oxygen plasma exposure, resulting in dangling bonds on the edges of the holes.[9,17] In all the devices fabricated using the *dual buffer layer* process, the unintentional severe doping by CHF_3 RIE processes observed in previous studies[9] is effectively minimized allowing reliable evaluation of G_{ON}/G_{OFF} values. Figure 3b shows the measured G_{ON}/G_{OFF} values as *w* decreases from 14.1 to 7.5 nm. OFF conductance (G_{OFF}) and ON conductance (G_{ON}) were evaluated at the Dirac point (V_{Dirac}) and at $V_G = V_{Dirac} - 45$ V, respectively, in a conductance curve as a function of gate bias. The FETs showed a modest increase in the G_{ON}/G_{OFF} of ~10 when compared to pristine CVD graphene when 11 nm < *w* < 15 nm. As *w* dips below 11 nm, the G_{ON}/G_{OFF} increases above 15. A further decrease in *w* to 7.5 nm increases the observed G_{ON}/G_{OFF} to ~24 ± 2. It should be noted that if we define ON/OFF conductance modulation based on the ratio of maximum conductance to minimum conductance in the conductance *versus* gate voltage plot in voltage range of $-40\ \text{V} < V_G < 40$ V, we obtained a higher value of 48 ± 4 at *w* = 7.5 nm.

It has been shown that graphene antidot lattice has a band gap, which increases as *w* decreases due to the quantum confinement effect.[9,10,19,20] NP graphene can be defined as an interconnected network of GNRs with electronic transport properties similar to GNRs.[9,10,19,20] The G_{ON}/G_{OFF} increase with decreasing *w* is consistent with the increase of an effective gap, which is the result of a combination of effects due to changes in band structure and the formation of a mobility gap induced by localized electronic states.[19,20,26,27] Both effects can result in an activated conduction mechanism in graphene, where the OFF conductance decreases exponentially with the temperature.[19,28] Hence, fitting G_{ON}/G_{OFF} data to the equation $G_{ON}/G_{OFF} = B \cdot \exp(A/(w \cdot 2k_BT))$, where *w* is the nanoconstriction width, k_B is Boltzmann constant and *T* is the temperature, gave coefficients *A* and *B* of 1.17 eV·nm and 1.35, respectively, showing excellent fit with the equation. Although this equation does not take into account all of the complex physics occurring in nanostructured graphene,[27,28] it is still appropriate as it fits experimental data of different nanostructured graphene well and therefore it captures the aggregate effect of all the complexities.[29] Further comparison of these measured values of G_{ON}/G_{OFF} with those compiled from all the literature reports on NP graphene irrespective of the fabrication method shows good agreement.[9,10,18−20] (Supporting Information, Figure S2) The G_{ON}/G_{OFF} of ~40 should roughly correspond to an effective band gap of ~100 meV based on measurements on NP graphene FET with the same periodicity previously reported by us.[9] Note that actual *w* of NP graphene in the report[9] could not be measured due to difficulty in removal of the overlying oxide and cross-linked polymer. The measured *w* (18 nm) was from patterned highly ordered pyrolytic graphite. It is likely that the resulting overetched NP graphene exhibited a *w* < 18 nm, similar to the previous reports on GNRs fabricated with silsesquioxane resist pattern.[11,30]

Degradation of Mobility in NP Graphene with Decrease in *w*. The reactive ion etching process is known to degrade the mobility of nanopatterned graphene. To access the extent of degradation in mobility with shrinking *w*, we calculated the hole mobility of fabricated FETs using a standard transistor model, $\mu = gL/V_{SD}C_{OX}W$, where *g* is the transconductance, *L* and *W* are the channel length and width of the fabricated device, respectively, V_{SD} is the source-drain potential, and C_{OX} is the gate capacitance per unit area. The large-area (>1 cm^2) of the fabricated samples allows the definition of large electrodes with regular channel geometry (L = 15 μm and W = 120 μm), which is critical to evaluating device performance. Prior to patterning, pristine CVD graphene FET devices showed a hole mobility of 500−1000 cm^2/(V·s), which is typical for CVD grown graphene.[31] Post nanopatterning, the hole mobility decreased markedly with a concomitant increase in G_{ON}/G_{OFF}. As shown in Figure 3b, for the devices with 8.7 nm < *w* < 15 nm, the measured hole mobilities are 7−20 cm^2/(V·s), which is dramatically lower than pristine graphene. A further decrease in *w* to 7.5 nm led to a much reduced mobility of ~0.12 cm^2/(V·s). Note that the electrical transport measurements are intended for and only capable of testing the macroscopic properties of the NP graphene over many periodicities of the BCP pattern. We use a parallel plate capacitance which slightly overestimates the capacitance, after taking into account fringe fields,[32] resulting in a slight underestimation of the bulk electrical mobility. Because of the inherent crystal grain boundary in the CVD grown graphene as well as variations in growth directions along the crystal lattice of the catalytic metal substrate, the mobility of CVD grown graphene is typically 1−2 orders of magnitude lower than that of mechanically exfoliated graphene.[31,33] The grain boundaries in CVD grown graphene are essentially retained in the lattice of patterned graphene, possibly contributing to significant mobility degradation. More importantly, the mobility of nanopatterned graphene is limited by charge carrier scattering caused by several possible factors which include, line edge roughness, interior defects, disordered edges, ionized impurities and acoustic and optical phonons.[34,35] Experimentally, Wang *et al*. reported that the mobility of chemically derived GNRs with smooth edges was 50−200 cm^2/(V·s) at $w \approx$ 1.5−3 nm.[36] Compared to this, lithographically patterned GNRs exhibited much lower mobility. For example, Murali *et al*. demonstrated that the mobility in lithographically patterned GNRs decreases to <200 cm^2/(V·s) when *w* < 20 nm. They attributed the mobility limitation in top-down etched GNRs to line edge roughness scattering.[37,38] Similarly, the top-down etching method used in our studies can also lead to line edge roughness and disordered edges as well as plasma induced dangling bonds, all of which degrade mobility. Therefore, it is crucial to understand the defects near the edges of NP graphene and its relationship to the fabrication method.

Raman Studies: Doping and Defects in NP Graphene. To understand electronic structure and defects in NP graphene, we utilized Raman spectroscopy, which is a powerful tool to analyze disorder and doping behavior in graphene.[39,40] Figure 4a shows representative Raman spectra from NP graphene with *w* ranging from 13.0 to 7.5 nm. For all samples, the G and 2D bands appear at ~1590 and ~2636 cm^{-1}, which correspond to optical E_{2g} phonon mode at the center of Brillouin zone and the second order peak of D band, respectively. Two additional defect-induced D and D′ bands were detected at ~1330 and ~1620 cm^{-1}, respectively, possibly due to defects in the graphene crystal.[40]

The position of G band is very sensitive to the local doping level in graphene.[41,42] Typically, a G band of undoped pristine graphene appears at 1581−1585 cm^{-1}. After nanopatterning, there is a systematic upshift in the position of G band with decreasing *w*. (Supporting Information, Figure S3) For example, the G band position for *w* of 13.1 and 7.5 nm were observed at ~1586 cm^{-1} and ~1593 cm^{-1}, respectively. The upshift in the G band further confirms increased hole-doping by oxygen dangling bonds with decreasing *w*, agreeing with the analysis of the conductance vs gate voltage curves discussed earlier as well as reports on G band shifts of patterned graphenes *via* O_2 plasma etching.[17,30]

Raman features of disordered carbonaceous materials have been studied extensively to gain insight into defects in the lattice.[40] The integrated intensity ratio of the D band and G band, I_D/I_G, is a parameter sensitive to defect density.[43−45] I_D/I_G as a function of *w* (Figure 4b) for NP graphene shows a similar scaling behavior to I_D/I_G values from lithographically fabricated GNR.[30] For lithographically patterned GNR, I_D/I_G increases with a decrease in *w* and reaches a maximum at *w* of 15 nm, whereas further decreasing *w* to 5 nm decreases I_D/I_G. In our studies on NP graphene, the maximum of I_D/I_G is 10.3 at a *w* of 13.0 nm. As *w* decreases further to 7.1 nm, I_D/I_G decreases to 4.2. Although it is difficult to directly compare all the values due to their different shape factors, that is, GNRs *versus* NP graphenes with different periodicity, by compiling I_D/I_G values from literature on NP graphenes[19,29] and GNRs[30,46] with our data on NP graphene as a function of *w*, three distinct regimes can be identified (Figure 4b): the increase in I_D/I_G by shrinking *w* from bulk to 13.0 nm (regime 1), the maximum I_D/I_G at 13.0 nm (regime 2), and the decrease in I_D/I_G for *w* less than 13.0 nm (regime 3). (Note that all the literature values were reported with the same laser wavelength, 633 nm, in this work.)

In previous studies of graphene with random defects generated by plasma or ion bombardment, a similar decrease in I_D/I_G has been observed and interpreted using a local defect activation model of D band.[44,45] In the Raman scattering process, the electron−hole pair generated by the Raman excitation travels a certain distance, called as Raman relaxation length (λ), before inelastic scattering occurs.[47] For NP

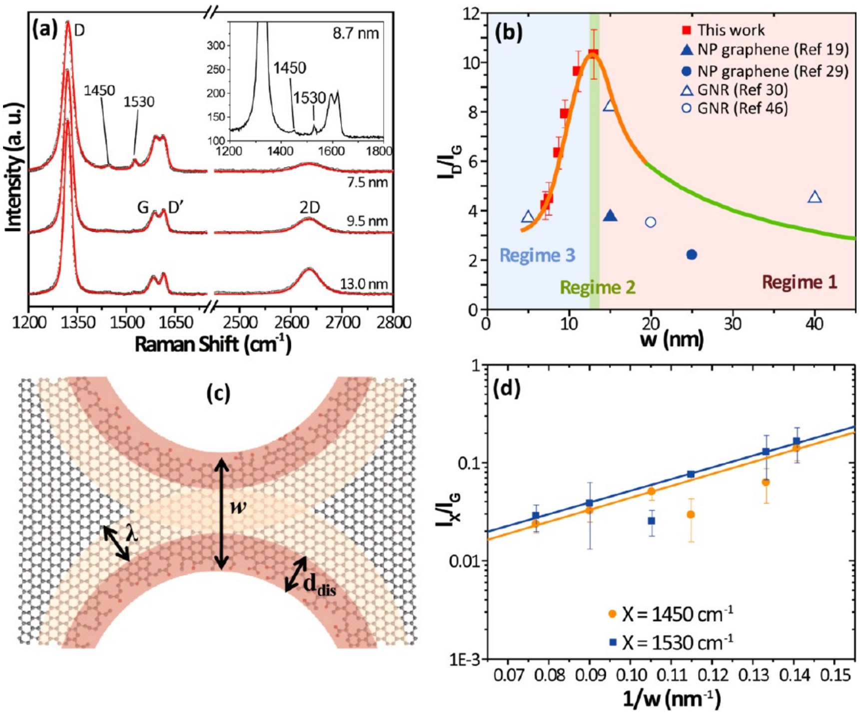

Figure 4. Raman characterization of nanoperforated graphene showing (a) the spectra as a function of *w* with the inset showing zoom in for *w* = 8.7 nm in 1200−1800 cm^{-1} range. (b) Extracted I_D/I_G values as a function of *w*. Red filled squares represent I_D/I_G from nanoperforated graphene *via* dual buffer layer process. Solid blue symbols[19,29] and open blue symbols[30,46] represent literature values of NP graphenes and GNRs, respectively. Green solid line is a fit curve with the literature values in 20 nm < *w* < 350 nm using $I_D/I_G \propto 1/w$.[29] Orange solid line is a guide to the eye for *w* < 20 nm. (c) Schematic showing local defect activation model (regime 3) for nanoperforated graphene, where Raman relaxation length is λ, and the width of disordered area is d_{dis}. In regime 3, defect activated regions by both edges coalesce, resulting in the decrease of I_D/I_G. (d) Semilog plot of I_X/I_G (X = 1450 cm^{-1}, orange trace; or X = 1530 cm^{-1}, blue trace) as a function of reciprocal *w*.

graphene, the edges of the holes are the origin of the D band, thus the electron−hole pair generated at the edges will travel over λ and form activated regions which enhance the D band scattering. In regime 1, $2\lambda + 2d_{dis} < w$, where d_{dis} is the distance of the disordered area created by O_2 plasma etching (∼ 2 nm).[11,30] As *w* shrinks, the area of the activated region increases while that of the unaffected region in the graphene lattice decreases, leading to an increase in the I_D/I_G ratio. However, as *w* keeps decreasing, the defect activated regions from different edges coalesce together (regime 3, $2\lambda + 2d_{dis} > w$, represented in Figure 4c), and the Raman excited electrons from either edge are indistinguishable and appear as one large defect activated region.[43−45] This coalescence leads to a decrease in the I_D/I_G ratio in regime 3. If the maximum of I_D/I_G is considered at ∼13.0 nm (which equals to $2\lambda + 2d_{dis}$), the estimated Raman relaxation length is ∼4 nm. Recent theoretical and experimental reports on the edges of graphene sheets and GNRs have suggested a Raman relaxation length of 2−5 nm, which is in good agreement with our results here on patterned graphene.[30,47] Considering randomized point defects in the graphene lattice, the maximum value of I_D/I_G from the literature appears at an interdefect distance of ∼3 nm,[43] which is significantly different from the maximum of I_D/I_G at 13.0 nm in this study. This difference suggests that the observed I_D/I_G behavior from NP graphene is not mainly due to randomized interior defects but most likely attributed to disordered edges created by top-down O_2 RIE. Hence, the low hole mobility measured in the FETs is due to highly disordered defects created near the edges, possibly, line edge roughness and edge defects including oxygen dangling bonds. Therefore, to achieve a smooth single edge structure, that is, zigzag or armchair, the approaches based on top-down[48−51] or bottom-up[29] methods have been studied.

As seen in Figure 4a, nanopatterning induces broader and less intense 2D band peak as *w* decreases.[52] Combining the changes in 2D band with measured mobilities from electrical characterization, we find that the full width at half-maximum of 2D band (fwhm(2D)) in Raman spectra correlates well with hole mobility. Fitting the data to the equation $\mu = a \cdot \exp(b \cdot \text{fwhm(2D)})$, where μ is the hole mobility, gave fitting coefficients of *a* and *b* of 4.41 × 10^5 and −0.21, respectively (Supporting Information, Figure S6). Robinson *et al.* reported that an increase in the fwhm(2D) can be correlated with carrier mobility degradation in epitaxial graphene.[53] As epitaxial graphene has a significant variation in the layer stacking, fwhm(2D) becomes broader and carrier mobility degrades, following the same equation above that was used for the fitting.

Our finding suggests that, in nanopatterned graphene, fwhm(2D) is also a Raman characteristic signature to probe electronic transport properties in a nondestructive and rapid manner.

Raman Studies: Edge Phonon Peaks at ~1450 cm^{-1} and ~1530 cm^{-1}. In the Raman spectra, we observed two well-defined sharp peaks at ~1450 and ~1530 cm^{-1} with a line width of ~10 cm^{-1}. The intensity of these peaks scales inversely with w. NP graphene with $w < 9$ nm exhibited particularly well-resolved peaks (Figure 4a). The 1450 cm^{-1} peak can be assigned to either the third order Raman scattering peak from silicon in the SiO_2/Si substrate,[25,47,54] the $\delta(CH_2)$ of any residual PS after processing[55] or the δ_a(C−H) of α-CH_3, δ_a(C−H) of O−CH_3 of PMMA.[56] We conducted Raman measurements on SiO_2/Si substrate and PS layer with patterned hole arrays on SiO_2/Si substrate without graphene. As shown in Supporting Information, Figure S4a, no sharp peaks were observed at 1450 and 1530 cm^{-1} from the SiO_2/Si substrate as well as patterned PS/SiO_2/Si. The peak at 1450 cm^{-1} from a PMMA sample is typically too broad (line width ~33 cm^{-1}, Supporting Information, Figure S4b), and PMMA cylindrical domains were completely removed during UV degradation and RIE processes. Hence, the observed sharp peaks at 1450 and 1530 cm^{-1} arise exclusively from the NP graphene, itself, and were assigned to the vibrational modes of edge atoms for H-terminated zigzag and armchair edges, respectively.[25,57] In a recent report, these two peaks were also observed in GNR samples by using a Raman enhancement technique called surface and interference co-enhanced Raman scattering (SICERS).[25] Using the SICERS technique, two sharp characteristic peaks at 1450 and 1530 cm^{-1} (line width ~7 cm^{-1}) were found with a 633 nm excitation laser from both monolayer or few-layer GNR samples fabricated by mechanical exfoliation or chemical exfoliation of graphite. In our studies on NP graphene, these two peaks are discernible without any Raman enhancement due to a much higher density of nanoconstriction in the Raman probe area. Coexistence of the two peaks shows that nanopatterning using RIE creates zigzag and armchair edges in addition to disordered edge defects including oxygen dangling bonds. The relative intensity ratio of 1450 and 1530 cm^{-1} bands to G band (I_X/I_G, X = 1450 or 1530 cm^{-1}) increases with decreasing w. (Figure 4d) For GNRs of $w > 20$ nm, I_X/I_G increases as the ribbon width decreases, and follows the relationship $I_X/I_G \approx E\cdot(1/w)$ where E is a constant.[25] In our system, the I_X/I_G is also a function of $^1/_w$ but follows the relationship $I_X/I_G \approx C\cdot\exp(D/w)$, where C and D are fitting constants. The reason for this discrepancy is not entirely clear to us, but it is possible that I_X/I_G follows a different width-dependence for $w < 20$ nm. Hence, in principle it is possible that the intensity of edge peaks can be used to estimate the width as well as to evaluate the structural quality of edge.

CONCLUSION

In summary, we have fabricated and characterized a stand alone large-area (>1 cm^2) NP graphene with a systematic variation in nanoconstriction width from 14 to 7.5 nm. These semiconducting graphene structures were fabricated using P(S-*b*-MMA) block copolymer template and a process that uses a sacrificial polymer layer on graphene. The sacrificial polymer layer serves the purpose of avoiding direct contact of etchants with graphene and enables clean isolation of the patterned graphene from the polymeric templates. The fabrication method allowed experimental confirmation of the relationship between electronic conductance modulation and w using large-area NP structures. Electrical characterization of large-area NP graphene confirms that the ON/OFF conductance modulation scales inversely with w, indicating the formation of an effective gap due to a confinement effect. Electrical measurements and Raman spectra confirm that the fabricated NP graphene is p-doped, most likely from the oxygen dangling bonds in the edges of hole arrays, but the extent of doping is greatly reduced due to the modified BCP process. From the variation of I_D/I_G as a function of w from Raman characterization three distinct regimes were identified where the ratio increases, attains a peak value, and then decreases with decrease in w. These studies reveal that the D band arises primarily from the disordered edges in the hole arrays. Interestingly the large-area NP graphene enabled by this modified BCP lithography process resulted in observable edge phonon peaks without the need for Raman enhancement. These studies confirm the coexistence of zigzag and armchair edge structures. From these comprehensive studies, we have shown that both electronic transport and Raman characteristics change in a concerted manner as w shrinks. These studies have been made possible by the fabrication of large-area NP graphene *via* the dual buffer layer process. In addition, it is feasible to further engineer the edge structure of fabricated NP graphene to attain a smooth single edge structure potentially using anisotropic etching methods.[48−51]

MATERIALS AND METHODS

Large-Area Graphene Synthesis and Transfer to SiO_2/Si Substrate. CVD graphene formation on Cu foil. Cu foil (Alfa Aesar, product no. 13382) was loaded into a horizontal, 28 mm diameter quartz tube furnace, which was heated to 1050 °C under a 900 sccm flow of forming gas (95% Ar, 5% H_2). After annealing for 30 min, 10 ppm of CH_4 was introduced into the flow and graphene was allowed to grow for 16 h, followed by quickly cooling

(~10 °C/sec until below 700 °C). Synthesized graphene was transferred from Cu foil by spin-coating PMMA (Microchem, 950 PMMA 2C) and backside-etching with an aqueous solution of 0.2 M HCl, 0.2 M $FeCl_3$. Floating film was washed by floating on 1:9 HF (49%)/DI water and subsequent floating on DI water, and allowed to dry on a 89 nm SiO_2/Si (p++) wafer. The PMMA film was removed using boiling dichloromethane, and the sample was further washed with isopropyl alcohol. Prior to patterning, average I_D/I_G of pristine CVD graphene from Raman spectra was 0.069 ± 0.058.

Nanopatterning Process. A 38 nm thick PS thin film (M_n = 20 000 g/mol) was deposited by spin-coating onto CVD grown SLG on 89 nm SiO_2/Si (p++) wafers and baking at 140 °C for 5 min. A 10 nm silicon oxide layer was deposited onto a PS coated graphene sample from a SiO_2 source by e-beam evaporation. A preassembled thin film of P(S-*b*-MMA) (M_n(PS) = 46k, M_n(PMMA) = 21k, PDI = 1.09) with PMMA cylindrical structure was deposited onto a silicon oxide/PS/SLG/substrate. The sample was then exposed to UV illumination (1000 mJ/cm^2) to selectively degrade the PMMA cylinders. The PMMA residue was removed by dipping the samples in acetic acid for 2 min and rinsing with DI water. A 50 W O_2 plasma RIE was utilized to remove residues inside the holes and the underlying random copolymer layer. A 300 W CHF_3(45 sccm)/O_2(5 sccm) mixed gas plasma was then utilized to etch the silicon oxide hardmask. Subsequently, the underlying PS layer and graphene were patterned using 20 W O_2 plasma. A 1% HF aqueous solution was used to remove the silicon oxide on the PS layer. Organic solvents (*N*-methyl-2-pyrrolidone and tetrahydrofuran) or commercial photoresist stripper (AZ-300T or AZ-400T) were used to remove the etched PS residue. Resulting samples were washed further with isopropyl alcohol and DI water.

Characterization. Imaging was conducted using LEO-1550VP field-emission scanning electron microscopy at 1−5 kV of accelerating voltage. Raman spectroscopy measurements were performed using Aramis Horiba Jobin Yvon Confocal Raman Microscope with 633 nm excitation laser and probing size of ~1 μm^2. For each sample, ~10 spectra were collected from different positions. All spectra were deconvoluted by fitting with Voigt function and characteristic peaks were identified. For electrical measurements, electrodes (50 nm Au) and a sacrificial mask (50 nm Cu) for the graphene channels were defined on fabricated NP graphene samples by thermal evaporation, utilizing a shadow mask. Exposed graphene was etched using a 50 W O_2 plasma for 20 s, followed by removal of the sacrificial mask in the copper etchant, resulting in 15 μm × 120 μm (length × width) graphene transistors. For each sample, 8−12 transistor devices were characterized, and average values with corresponding standard deviation values were reported.

Conflict of Interest: The authors declare no competing financial interest.

Acknowledgment. This research was funded by the National Science Foundation. (Grant No. CMMI-1129802) E.H. acknowledges partial support from the National Science Foundation-Nanoscale Science and Engineering Center at the University of Wisconsin-Madison. (Grant No. DMR-0832760) We acknowledge the support from the staff and the use of equipments at the Materials Science Center, Wisconsin Center for Microelectronics, the Center for Nanotechnology and the Synchrotron Radiation Center at the University of Wisconsin. (National Science Foundation Grant No. DMR-0537588)

Supporting Information Available: Supporting figures as described in the text. This material is available free of charge *via* the Internet at http://pubs.acs.org.

REFERENCES AND NOTES

1. Lin, Y.-M.; Jenkins, K. A.; Valdes-Garcia, A.; Small, J. P.; Farmer, D. B.; Avouris, P. Operation of Graphene Transistors at Gigahertz Frequencies. *Nano Lett.* **2009**, *9*, 422–426.
2. Lin, Y.-M.; Valdes-Garcia, A.; Han, S.-J.; Farmer, D. B.; Meric, I.; Sun, Y.; Wu, Y.; Dimitrakopoulos, C.; Grill, A.; Avouris, P.; *et al.* Wafer-Scale Graphene Integrated Circuit. *Science* **2011**, *332*, 1294–1297.
3. Hecht, D. S.; Hu, L.; Irvin, G. Emerging Transparent Electrodes Based on Thin Films of Carbon Nanotubes, Graphene, and Metallic Nanostructures. *Adv. Mater.* **2011**, *23*, 1482–1513.
4. Bae, S.; Kim, H.; Lee, Y.; Xu, X.; Park, J.-S.; Zheng, Y.; Balakrishnan, J.; Lei, T.; Kim, H. R.; Song, Y. I.; *et al.* Roll-to-roll Production of 30-in. Graphene Films for Transparent Electrodes. *Nat. Nanotechnol.* **2010**, *5*, 574–578.
5. Bonaccorso, F.; Sun, Z.; Hasan, T.; Ferrari, A. C. Graphene Photonics and Optoelectronics. *Nat. Photon.* **2010**, *4*, 611–622.
6. Kim, K. S.; Zhao, Y.; Jang, H.; Lee, S. Y.; Kim, J. M.; Kim, K. S.; Ahn, J.-H.; Kim, P.; Choi, J.-Y.; Hong, B. H. Large-Scale Pattern Growth of Graphene Films for Stretchable Transparent Electrodes. *Nature* **2009**, *457*, 706–710.
7. Geim, A. K. Graphene: Status and Prospects. *Science* **2009**, *324*, 1530–1534.
8. Schwierz, F. Graphene Transistors. *Nat. Nanotechnol.* **2010**, *5*, 487–496.
9. Kim, M.; Safron, N. S.; Han, E.; Arnold, M. S.; Gopalan, P. Fabrication and Characterization of Large-Area, Semiconducting Nanoperforated Graphene Materials. *Nano Lett.* **2010**, *10*, 1125–1131.
10. Bai, J.; Zhong, X.; Jiang, S.; Huang, Y.; Duan, X. Graphene Nanomesh. *Nat. Nanotechnol.* **2010**, *5*, 190–194.
11. Han, M. Y.; Özyilmaz, B.; Zhang, Y.; Kim, P. Energy Band-Gap Engineering of Graphene Nanoribbons. *Phys. Rev. Lett.* **2007**, *98*, 206805.
12. Jiao, L.; Zhang, L.; Wang, X.; Diankov, G.; Dai, H. Narrow Graphene Nanoribbons from Carbon Nanotubes. *Nature* **2009**, *458*, 877–880.
13. Kosynkin, D. V.; Higginbotham, A. L.; Sinitskii, A.; Lomeda, J. R.; Dimiev, A.; Price, B. K.; Tour, J. M. Longitudinal Unzipping of Carbon Nanotubes to Form Graphene Nanoribbons. *Nature* **2009**, *458*, 872–876.
14. Bai, J.; Duan, X.; Huang, Y. Rational Fabrication of Graphene Nanoribbons Using a Nanowire Etch Mask. *Nano Lett.* **2009**, *9*, 2083–2087.
15. Li, X.; Wang, X.; Zhang, L.; Lee, S.; Dai, H. Chemically Derived, Ultrasmooth Graphene Nanoribbon Semiconductors. *Science* **2008**, *319*, 1229–1232.
16. Bai, J.; Huang, Y. Fabrication and Electrical Properties of Graphene Nanoribbons. *Mater. Sci. Eng., R* **2010**, *70*, 341–353.
17. Heydrich, S.; Hirmer, M.; Preis, C.; Korn, T.; Eroms, J.; Weiss, D.; Schüller, C. Scanning Raman Spectroscopy of Graphene Antidot Lattices: Evidence for Systematic P-type Doping. *Appl. Phys. Lett.* **2010**, *97*, 043113.
18. Sinitskii, A.; Tour, J. M. Patterning Graphene through the Self-Assembled Templates: Toward Periodic Two-Dimensional Graphene Nanostructures with Semiconductor Properties. *J. Am. Chem. Soc.* **2010**, *132*, 14730–14732.
19. Safron, N. S.; Brewer, A. S.; Arnold, M. S. Semiconducting Two-Dimensional Graphene Nanoconstriction Arrays. *Small* **2010**, *7*, 492–498.
20. Liang, X.; Jung, Y.-S.; Wu, S.; Ismach, A.; Olynick, D. L.; Cabrini, S.; Bokor, J. Formation of Bandgap and Subbands in Graphene Nanomeshes with Sub-10 nm Ribbon Width Fabricated *via* Nanoimprint Lithography. *Nano Lett.* **2010**, *10*, 2454–2460.
21. Stoykovich, M. P.; Nealey, P. F. Block Copolymers and Conventional Lithography. *Mater. Today* **2006**, *9*, 20–29.
22. Occhielloa, E.; Morraa, M.; Cinquinaa, P.; Garbassi, F. Hydrophobic Recovery of Oxygen-Plasma-Treated Polystyrene. *Polymer* **1992**, *33*, 3007–3015.
23. Hong, A. J.; Liu, C.-C.; Wang, Y.; Kim, J.; Xiu, F.; Ji, S.; Zou, J.; Nealey, P. F.; Wang, K. L. Metal Nanodot Memory by Self-Assembled Block Copolymer Lift-Off. *Nano Lett.* **2010**, *10*, 224–229.
24. Jeong, S.-J.; Kim, J. E.; Moon, H.-S.; Kim, B. H.; Kim, S. M.; Kim, J. B.; Kim, S. O. Soft Graphoepitaxy of Block Copolymer Assembly with Disposable Photoresist Confinement. *Nano Lett.* **2009**, *9*, 2300–2305.
25. Ren, W.; Saito, R.; Gao, L.; Zheng, F.; Wu, Z.; Liu, B.; Furukawa, M.; Zhao, J.; Chen, Z.; Cheng, H.-M. Edge Phonon

State of Monolayer and Few-Layer Graphene Nanoribbons Observed by Surface and Interference Co-enhanced Raman Spectroscopy. *Phys. Rev. B: Condens. Matter* **2010**, *81*, 035412.

26. Safron, N. S.; Arnold, M. S. Characterization of Conduction Mechanism Relevant to Device Performance in Nanoperforated Graphene. *Int. J. High Speed. Electr. Syst.* **2011**, *20*, 697–706.
27. Stampfer, C.; Güttinger, J.; Hellmüller, S.; Molitor, F.; Ensslin, K.; Ihn, T. Energy Gaps in Etched Graphene Nanoribbons. *Phys. Rev. Lett.* **2009**, *102*, 056403.
28. Shimizu, T.; Haruyama, J.; Marcano, D. C.; Kosinkin, D. V.; Tour, J. M.; Hirose, K.; Suenaga, K. Large Intrinsic Energy Bandgaps in Annealed Nanotube-Derived Graphene Nanoribbons. *Nat. Nanotechnol.* **2011**, *6*, 45–50.
29. Safron, N. S.; Kim, M.; Gopalan, P.; Arnold, M. S. Barrier-Guided Growth of Micro- and Nano-Structured Graphene. *Adv. Mater.* **2012**, *24*, 1041–1045.
30. Ryu, S.; Maultzsch, J.; Han, M. Y.; Kim, P.; Brus, L. E. Raman Spectroscopy of Lithographically Patterned Graphene Nanoribbons. *ACS Nano* **2011**, *5*, 4123–4130.
31. Reina, A.; Jia, X.; Ho, J.; Nezich, D.; Son, H.; Bulovic, V.; Dresselhaus, M. S.; Kong, J. Large Area, Few-Layer Graphene Films on Arbitrary Substrates by Chemical Vapor Deposition. *Nano Lett.* **2009**, *9*, 30–35.
32. Lin, Y.-M.; Perebeinos, V.; Chen, Z.; Avouris, P. Electrical Observation of Subband Formation in Graphene Nanoribbons. *Phys. Rev. B: Condens. Matter* **2008**, *78*, 161409.
33. Li, X.; Magnuson, C. W.; Venugopal, A.; An, J.; Suk, J. W.; Han, B.; Borysiak, M.; Cai, W.; Velamakanni, A.; Zhu, Y.; *et al.* Graphene Films with Large Domain Size by a Two-Step Chemical Vapor Deposition Process. *Nano Lett.* **2010**, *10*, 4328–4334.
34. Betti, A.; Fiori, G.; Iannaccone, G.; Mao, Y. Physical Insights on Graphene Nanoribbon Mobility through Atomistic Simulations. *IEDM Tech. Dig.* **2009**, 897–900.
35. Betti, A.; Fiori, G.; Iannaccone, G. Atomistic Investigation of Low-Field Mobility in Graphene Nanoribbons. *IEEE Trans. Electron Devices* **2011**, *58*, 2824–2830.
36. Wang, X.; Ouyang, Y.; Li, X.; Wang, H.; Guo, J.; Dai, H. Room-Temperature All-Semiconducting Sub-10-nm Graphene Nanoribbon Field-Effect Transistors. *Phys. Rev. Lett.* **2008**, *100*, 206803.
37. Bryan, S. E.; Yang, Y.; Murali, R. Conductance of Epitaxial Graphene Nanoribbons: Influence of Size Effects and Substrate Morphology. *J. Phys. Chem. C* **2011**, *115*, 10230–10235.
38. Yang, Y.; Murali, R. Impact of Size Effect on Graphene Nanoribbon Transport. *IEEE Electron Device Lett.* **2010**, *31*, 237–239.
39. Dresselhaus, M. S.; Jorio, A.; Saito, R. Characterizing Graphene, Graphite, and Carbon Nanotubes by Raman Spectroscopy. *Annu. Rev. Condens. Matter Phys.* **2010**, *1*, 89–108.
40. Ferrari, A. C. Raman Spectroscopy of Graphene and Graphite: Disorder, Electron-Phonon Coupling, Doping and Nonadiabatic Effects. *Solid State Commun.* **2007**, *143*, 47–57.
41. Pisana, S.; Lazzeri, M.; Casiraghi, C.; Novoselov, K. S.; Geim, A. K.; Ferrari, A. C.; Mauri, F. Breakdown of the Adiabatic Born-Oppenheimer Approximation in Graphene. *Nat. Mater.* **2007**, *6*, 198–201.
42. Das, A.; Pisana, S.; Chakraborty, B.; Piscanec, S.; Saha, S. K.; Waghmare, U. V.; Novoselov, K. S.; Krishnamurthy, H. R.; Geim, A. K.; Ferrari, A. C.; *et al.* Monitoring Dopants by Raman Scattering in an Electrochemically Top-Gated Graphene Transistor. *Nat. Nanotechnol.* **2008**, *3*, 210–215.
43. Cançado, L. G.; Jorio, A.; Ferreira, E. H. M.; Stavale, F.; Achete, C. A.; Capaz, R. B.; Moutinho, M. V. O.; Lombardo, A.; Kulmala, T. S.; Ferrari, A. C. Quantifying Defects in Graphene *via* Raman Spectroscopy at Different Excitation Energies. *Nano Lett.* **2011**, *11*, 3190–3196.
44. Lucchese, M. M.; Stavale, F.; Ferreira, E. H. M.; Vilani, C.; Moutinho, M. V. O.; Capaz, R. B.; Achete, C. A.; Jorio, A. Quantifying Ion-Induced Defects and Raman Relaxation Length in Graphene. *Carbon* **2010**, *48*, 1592–1597.
45. Luo, Z.; Yu, T.; Ni, Z.; Lim, S.; Hu, H.; Shang, J.; Liu, L.; Shen, Z.; Lin, J. Electronic Structures and Structural Evolution of Hydrogenated Graphene Probed by Raman Spectroscopy. *J. Phys. Chem. C* **2011**, *115*, 1422–1427.
46. Wang, X.; Dai, H. Etching and Narrowing of Graphene from the Edges. *Nat. Chem.* **2010**, *2*, 661–665.
47. Casiraghi, C.; Hartschuh, A.; Qian, H.; Piscanec, S.; Georgi, C.; Fasoli, A.; Novoselov, K. S.; Basko, D. M.; Ferrari, A. C. Raman Spectroscopy of Graphene Edges. *Nano Lett.* **2009**, *9*, 1433–1441.
48. Begliarbekov, M.; Sasaki, K.-I.; Sul, O.; Yang, E.-H.; Strauf, S. Optical Control of Edge Chirality in Graphene. *Nano Lett.* **2011**, *11*, 4874–4878.
49. Jia, X.; Hofmann, M.; Meunier, V.; Sumpter, B. G.; Campos-Delgado, J.; Romo-Herrera, J. M.; Son, H.; Hsieh, Y.-P.; Reina, A.; Kong, J.; *et al.* Controlled Formation of Sharp Zigzag and Armchair Edges in Graphitic Nanoribbons. *Science* **2009**, *323*, 1701–1705.
50. Shi, Z.; Yang, R.; Zhang, L.; Wang, Y.; Liu, D.; Shi, D.; Wang, E.; Zhang, G. Patterning Graphene with Zigzag Edges by Self-Aligned Anisotropic Etching. *Adv. Mater.* **2011**, *23*, 3061–3065.
51. Shimizu, T.; Nakamura, J.; Tada, K.; Yagi, Y.; Haruyama, J. Magnetoresistance Oscillations Arising from Edge-Localized Electrons in Low-Defect Graphene Antidot-Lattices. *Appl. Phys. Lett.* **2012**, *100*, 023104.
52. Bischoff, D.; Güttinger, J.; Dröscher, S.; Ihn, T.; Ensslin, K.; Stampfer, C. Raman Spectroscopy on Etched Graphene Nanoribbons. *J. Appl. Phys.* **2011**, *109*, 073710–073710.
53. Robinson, J. A.; Wetherington, M.; Tedesco, J. L.; Campbell, P. M.; Weng, X.; Stitt, J.; Fanton, M. A.; Frantz, E.; Snyder, D.; VanMil, B. L.; *et al.* Correlating Raman Spectral Signatures with Carrier Mobility in Epitaxial Graphene: A Guide to Achieving High Mobility on the Wafer Scale. *Nano Lett.* **2009**, *9*, 2873–2876.
54. Acker, W. P.; Yip, B.; Leach, D. H.; Chang, R. K. The Use of a Charge-Coupled Device and Position Sensitive Resistive Anode Detector for Multiorder Spontaneous Raman Spectroscopy from Silicon. *J. Appl. Phys.* **1988**, *64*, 2263–2270.
55. Jasse, B.; Chao, R. S.; Koenig, J. L. Laser Raman Scattering in Uniaxially Oriented Atactic Polystyrene. *J. Polym Sci, Polym. Phys. Ed.* **1978**, *16*, 2157–2169.
56. Willis, H. A.; Zichy, V. J. I.; Hendra, P. J. The Laser-Raman and Infra-red Spectra of Poly(methyl methacrylate). *Polymer* **1969**, *10*, 737–746.
57. Saito, R.; Furukawa, M.; Dresselhaus, G.; Dresselhaus, M. S. Raman Spectra of Graphene Ribbons. *J. Phys.: Condens. Matter* **2010**, *22*, 334203.